Measurement of shock structure and shock–vortex interaction in underexpanded jets using Rayleigh scattering

J. Panda[a)]
Modern Technologies Corporation, Middleburg Heights, Ohio 44130

R. G. Seasholtz
NASA Glenn Research Center, Cleveland, Ohio 44135

(Received 8 May 1998; accepted 20 August 1999)

The density field of underexpanded supersonic free jets issuing from a choked circular nozzle was measured using a Rayleigh scattering-based technique. This reliable and nonintrusive technique is particularly suitable for high-speed flows and is fundamentally superior to the intrusive probes and particle-based techniques such as laser Doppler velocimetry. A continuous wave laser and photon counting electronics were employed for time and phase-averaged density measurements. The use of dust-free air for the entrained flow allowed measurements in the shear layer region. The free jets were produced in the plenum to ambient pressure ratio range of 1.88–5.75, which corresponded to a fully expanded Mach number range of $0.99 \leqslant M_j \leqslant 1.8$. A comparative study of schlieren photographs and time-averaged density data provided insight into the shock-cell structures. The radial profiles obtained at various axial stations covering a downstream distance of 10 jet diameters show the development of the jet shear layer and the decay of the shock–cells. The supersonic free jets produced screech sound. A phase-averaged photon counting technique, using the screech tone as the trigger source, was used to measure the unsteady density variation. The phase-averaged density data show the evolution of the large-scale turbulent vortices that are found to be modulated periodically along the flow direction. A comparison with previously obtained data showing near-field pressure fluctuation and convective speed of the organized vortices reveals many interesting dynamics. All quantities show regular spatial modulation. The locations of local maxima in density fluctuations are found to coincide with the high convective speed and the antinode points in the near-field pressure fluctuation. Interestingly, the periodicity of modulation is found to be somewhat different from the shock spacing. Instead it shows that the standing wave system, known to exist in the near-field pressure fluctuation, extends into the jet shear layer. The standing wave is formed between the downstream moving Kelvin–Helmholtz instability waves and the upstream propagating part of sound waves. A detailed field measurement of the unsteady density fluctuation was conducted for the $M_j = 1.19$ and 1.42 jets for which the near-field pressure fluctuation data were obtained previously. The phase-matched, combined plots of the density fluctuation present inside the jet flow, and the pressure fluctuation present just outside the jet boundary provide a charming insight into the shock–vortex interaction leading to the sound wave generation. © *1999 American Institute of Physics.* [S1070-6631(99)01712-2]

I. INTRODUCTION

Although supersonic underexpanded free jets are found in many applications involving jet and rocket propulsion, our knowledge of the flow field has remained incomplete. Information about various fluid dynamic quantities, such as the density, temperature of velocity distribution, is obtained from computational fluid dynamics (CFD) efforts.[1–4] A lack of quantitative experimental data has compelled comparison of the CFD results with schlieren visualization[4] which is qualitative at best. The present study is a part of a screech noise program.[5–7] Underexpanded supersonic jets produce shock-associated noise, and screech tone is a special case in this noise category. From the earlier work of Powell[8] it is known that the screech generation is dependent on the shock-cell parameters, the interactions with the Kelvin–Helmholtz instability waves present in the shear layer and a self-sustaining feedback loop. It is odd to note that the vast majority of earlier work on screech has concentrated on the sound field while providing a superficial description of the flow field. This lack of reliable experimental data has compelled the existing screech prediction efforts (Cain *et al.*,[5] Tam *et al.*[9]) to extrapolate the known perfectly expanded jet data to determine the underexpanded jet flow fields. Since the flow field of a shock-containing underexpanded jet is expected to be vastly different from that of a perfectly expanded jet, the results obtained from the prediction efforts are also expected to be approximate. The motivation of the current experimental program is to measure the flow field of underexpanded jets using a nonintrusive technique and

[a)]Resident research associate at NASA Glenn Research Center, Cleveland, OH 44135. Corresponding author.

thereby advancing the fundamental understanding as well as providing a database that can be used for further refinements of the computational efforts.

The lack of experimental data is primarily due to the problems in using the traditional experimental tools. Insertion of any intrusive probe, such as the static and total pressure tubes or a hot-wire probe, changes the shock structure significantly. The present authors built a static pressure measuring probe similar to the one used in an earlier well-known study[10] and found out that the frequency and amplitude of the screech tone change dramatically as the probe is inserted into the flow. As the probe was moved downstream from a one shock cell to the next an edgetone-like staging characteristic was heard. All of these indicated significant alteration of the jet flow. An intrusive hot-wire probe has been used by Hu and McLaughlin[11] in a low Reynolds number jet to provide limited mass-flux fluctuation data. Laser Doppler velocimetry (LDV) is partially successful in providing time-averaged velocity data.[12,13] However, various problems associated with seed particles passing through shock waves, beam steering effects from sharp density gradients (in dual-beam technique), and problems in measuring high Doppler frequency shift using commercially available electronics make LDV difficult to apply. Similar problems associated with seeding particles are also encountered in the particle image velocimetry (PIV).[14,15] An additional problem of using a particle-based technique to measure turbulent shear flows arises from biasing effects. The Rayleigh scattering technique, on the other hand, depends on the light scattering from air molecules. Since no seed particles are used and only a single beam is necessary, many problem associated with LDV and PIV can be overcome. Moreover, information is obtained directly from the molecular distributions, therefore, the Rayleigh scattering technique is a more fundamental way of measuring flow properties. The ultimate purpose of the Rayleigh scattering setup is to obtain velocity and temperature data, in addition to the density data presented in this paper. In the past Rayleigh scattering has been used in various flow fields, such as to survey pocket plumes (Seasholtz *et al.*[16]), to measure time-averaged and unsteady gas concentration in premixed flames,[17–19] and recently to measure density in a turbine cascade.[20] Since it is relatively easy to produce a small supersonic jet in the laboratory environment, free jets have been common test grounds for various optical techniques including a few variations of the Rayleigh scattering-based techniques.[21–24] The velocity and density data reported in the above-mentioned studies are from a few points, and are insufficient to characterize the complete flow field, which is the motivation of the current study.

Some additional comments are necessary to clarify the background of the present work. An experimental program on screech noise is in progress at the NASA Glenn Research Center. As part of this program the oscillation of various shock waves (Panda[13]) and the near-field pressure fluctuations present just outside the jet boundary (Panda[25]) were also measured. However, the flow field information was limited. The goal of the present work is to complement the earlier studies by providing detailed flow field data. Therefore, a major part of the present experiment was conducted at the identical operating conditions of $M_j = 1.19$ and 1.42 for which the screech frequencies and modes are, respectively, 8400 Hz, axisymmetric and 5400 Hz, helical. The same jet facility and nozzle blocks used in the previous studies are used for the present one. A particularly useful result of the earlier studies is the data showing temporal evolution of the near-field pressure fluctuations. These data were obtained by phase averaging a microphone signal. Since a microphone can be used only outside the jet flow, the need for a new experimental tool capable of obtaining unsteady data inside the flow field becomes apparent. This has provided an additional motivation to extend the Rayleigh scattering technique to unsteady phase-averaged measurements. The technique developed for this purpose is discussed in the text, and the phase-matched, combined views of density fluctuation and near-field pressure fluctuations are also presented. It is worth adding here that the screech directiviety patterns for the same operating conditions were measured earlier by Lush and Burrin[26] and cine films from schlieren visualization were made by Westley and Wooley.[27] These references provide complimentary information to the present set of papers. It is hoped that the data set can be used as a standard to validate the current as well as the future computational and analytical efforts to predict screech and flow characteristics of underexpanded jets.

The reason for choosing the two operating Mach number conditions of $M_j = 1.19$ and 1.42 is that the screech tone, which for the most part is unsteady and appears in bursts,[28] becomes steady and regular at these windows. The axisymmetric nozzle geometry used for the present experiment produces ''cleaner'' flow compared to nonaxisymmetric (such as rectangular and elliptic) geometry where axis switching and corner vortices bring additional complexities.

Finally, an interesting observation in the screech sound generation process revealed in an earlier work[25] needs to be mentioned. In a screeching jet the strongest beam of sound propagates upstream toward the nozzle lip and self-excite the shear layer. As a result of this feedback loop the Kelvin–Helmholtz instability waves present in the shear layer become very coherent. They are referred to as the organized vortices. Unlike a perfectly expanded jet the rolled up vortices in a screeching jet are found to be periodically modulated. Although the intuitive expectations will be to see the spatial periodicity of modulation to be that of the shock spacing, in reality the periodicity is found to be slightly different. The spacing of the modulation follows that of a standing wave formed between the downstream propagating organized vortices and the upstream propagating screech waves. That this standing wave is present in the near-field region just outside the shear-layer boundary is a known fact. However, its presence inside the shear layer is a new observation. The present paper confirms this observation and further elaborates upon the implications in light of recent computations.[7]

Laser-induced Rayleigh scattering: When a laser beam is allowed to pass through a gas, the molecules present in the gas cause quasielastic light scattering. The scattered light, P_s, collected from a probe volume, V_{sc}, into a solid angle, $d\Omega$, can be written as (Seasholtz *et al.*[16])

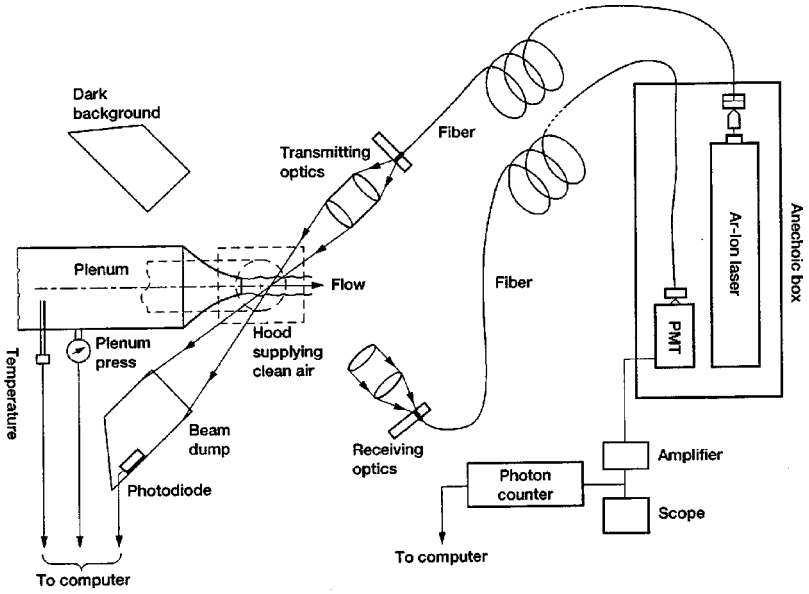

FIG. 1. Schematic of the Rayleigh scattering setup.

$$P_s = nI_0 V_{sc} \frac{d\sigma}{d\Omega} \sin^2 \kappa d\Omega = k' n, \tag{1}$$

where n is the molecular number density, I_0 is the incident light intensity, $d\sigma/d\Omega$ is the differential Rayleigh scattering cross-section of the gas (or gas mixture) under consideration, and κ is the angle between the incident electric vector and the direction of light collection. The Rayleigh scattering cross section depends on the light wavelength and the effective molecular diameter. This is constant for a fixed wavelength laser and a fixed gas mixture (air for this work). For a fixed optical setup, the scattered laser power is directly proportional to the molecular number density. Now, the number density, n, is related to the bulk density, ρ, through the following:

$$n = \frac{\rho N_A}{M}, \tag{2}$$

where M is the molecular weight and N_A is the Avogadro constant (6.022×10^{26} kmol^{-1}). The scattered light intensity was measured using a photomultiplier tube and a photon counting process was performed. The number of photons collected during a fixed time interval Δt can be written as

$$N = \frac{\epsilon P_s \Delta t}{h\nu} = \frac{\epsilon \rho N_A I_0 V_{sc} \frac{d\sigma}{d\Omega} \sin^2 \kappa d\Omega \Delta t}{Mh\nu} = k\rho \Delta t, \tag{3}$$

where h is the Planck constant, ν is the frequency of the laser light, and ϵ is the overall collection efficiency (a product of the light transmission efficiency and the quantum efficiency of the photomultiplier tube). Equation (3) shows that the photon count over a fixed time interval is directly proportional to the gas density at the probe volume. The proportionality constant has to be determined through a calibration process.

II. EXPERIMENTAL SETUP

The experiments were conducted at the NASA Glenn Research Center. Figure 1 shows a schematic of the experimental setup. Supersonic underexpanded jets were produced from a choked, 25.4-mm-diam circular nozzle in the pressure ratio range of 1.89–5.75. This paper follows a common practice of expressing the operating conditions in terms of a ''fully expanded Mach number,'' M_j, which is the ideal Mach number achievable by isentropically expanding the plenum pressure to the ambient value. The operating pressure ratios cover a fully expanded Mach number range of $1.0 \leqslant M_j \leqslant 1.8$. The details of the nozzle rig construction were presented earlier by Panda.[25] The supply air was unheated with an average total temperature of 24°C. This was also the average ambient temperature. The average ambient air density was 1.17 kg/m^3.

In essence, the Rayleigh scattering setup consists of a continuous laser beam focused at a point (probe volume) in the flow field, with the light scattered by the air molecules collected and measured by a photomultiplier tube. The green laser line (514.5 nm) from an argon-ion laser was used for the present experiment. Since the laser was kept in the same test cell with the nozzle rig, the extremely high noise level produced by supersonic jets was a concern for stable operation of the laser. Therefore, the laser and the optical measurement device were placed in an anechoic box, and the light was passed through 30-m-long, multimode, fiber optic cables. The setup facilitated stable operation of the laser and the light intensity was found to remain unchanged over 10 h of continuous operation. In the transmitting side, the optical train was designed to transmit laser light through a 0.365 mm core diameter fiber and focused at the measurement volume using an $f/2$, 80-mm-diam and an $f/3.3$, 82-mm-diam achromatic lenses. The scattered light was collected from a 90° angle using identical lenses and was coupled to a 0.55 mm core diameter fiber. The $f/3.3$ lens fixed the collection aperture. The laser power delivered to the probe volume was 0.65

W. However, the laser light at the probe volume was randomly polarized by its transmission through the optical fiber. Thus, because of the polarization sensitivity of the Rayleigh scattering [Eq. (1)], only about 1/2 of the laser power was effectively used. The core diameter of the collection fiber and the magnification factor of the collecting lenses fixed the probe volume length to 1.03 mm. The diameter of the beam waist was 0.16 mm. The scattered light was measured by a thermo-electrically cooled photomultiplier tube. The optical arrangement was designed to measure the axial velocity and temperature in addition to the density measurement performed for the present work.

To minimize stray light, the incident beam was directed into a beam dump. A similar arrangement was made in the collection side to provide a dark background. The transmitting and receiving optics, including the beam dump and the dark background, were mounted on a two-axis traversing mechanism that facilitated point by point movement along the flow (x axis) and transverse (r-axis) directions. The jet operating conditions were monitored via a pressure transducer and a thermocouple probe placed in the jet plenum.

The low level of the scattered light called for a photon counting system and the cooled photomultiplier tube (PMT) was especially suitable. A snubbing circuit was built at the PMT output to improve the shape of individual photon pulse. The output of this circuit was amplified by a wide bandwidth amplifier and the final counting was performed through a photon counter. A typical count rate obtained from the setup was 1.7×10^6/s.

A few other hurdles had to be overcome before the Rayleigh scattering technique could be successfully implemented. The most difficult one arose from the dust particles. Since particle (Mie) scattering is a few orders of magnitude stronger than the Rayleigh scattered light, the presence of dust particles can completely swamp the Rayleigh signature. The dry air, supplied to the rig from a central high pressure facility, was passed through two sets of filters for dust removal. This made the primary jet air very clean; however particles from the entrained air made density measurement impossible in the jet shear layer. To mitigate this problem, an air filter system that provided dust-free air in the jet neighborhood was installed. The clean air was routed via a flexible duct and exhausted vertically at a very low speed ($\sim$8 m/s) through a 30.5 cm$\times$38 cm hood over the nozzle block (Fig. 1). The clean air from the hood flows in a vertical direction, normal to the main jet, and in effect, creates a cross-flow situation. However, any perturbation to the supersonic jet is expected to be minimal due to the very low cross-flow velocity.

The second problem was with the stray reflected laser light. Due to the special 90° arrangement of the optical setup, the primary laser beam was found to intersect the nozzle block when the probe volume was close to the nozzle exit (within the first one-half diameter distance). In this region the stray background light overwhelmed the Rayleigh signature and no measurement was possible. Between 0.5D and 1.5D (D=nozzle exit diameter) downstream distance the stray light was still found to contaminate the Rayleigh light. The best way around this problem is to subtract the no flow photon count (N_{nf}) from the count obtained with the flow on (N_f) and then add a reference no flow count obtained from a far away point unaffected by the stray light (N_{ref}). Therefore, the corrected photon count (N_{cor}) is

$$N_{\mathrm{cor}}(x,r)=N_f(x,r)-N_{\mathrm{nf}}(x,r)+N_{\mathrm{ref}}. \tag{4}$$

Usually, the no flow counts were obtained from identical measurements stations immediately after obtaining the flow counts. The time-averaged data presented in this paper are corrected in this way, while the phase-averaged data are left uncorrected.

The third problem was with condensation. The primary supply air was dried to a dew point of -50 °C; therefore moisture condensation was absent in the primary air jet. However, the entrained room air contained a significant amount of moisture, which condensed in the shear layer and caused significant stray scattering. As the jet Mach number is increased the unheated air is cooled to a progressively lower temperature and the condensation appears closer to the nozzle exit. An effective solution is found in operating the jet for a couple of hours continuously before starting the data acquisition. The jet facility is located in a closed test cell and a couple of hours of operation purged the moist room air and significantly reduced condensation.

III. RESULTS AND DISCUSSION

A. Calibration

For the time-averaged data, photon counting was performed over a 4 s interval. A calibration process was necessary to determine the proportionality constant between the rate of photon count (N_r) and the air density, as well as to determine the residual stray light collected through the optics. Free jets at various known density conditions were obtained by changing the plenum pressure, P_0. The air density at the jet core (ρ_j) can be determined from isentropic relation until a choked condition (jet Mach number $M_j \leqslant 1$) is reached:

$$\rho_j=\frac{P_0}{RT_0}\left(\frac{P_0}{P_{\mathrm{amb}}}\right)^{-1/\gamma}, \tag{5}$$

where T_0 is the plenum temperature, P_{amb} is the ambient pressure, R is the universal gas constant, and γ is the ratio of specific heats. The photon arrival rate was counted at each operating condition and a straight line,

$$N_r=k\rho_j+B, \tag{6}$$

was fitted through the data (Fig. 2) using the least-squares method. The slope of the line, k, provided the proportionality constant as shown in Eq. (3), and the intercept, B, provided a measure of the stray light. Using a standard deviation of 1%, the goodness of fit was established to be 1.0. It should be pointed out that the density variations, encountered in the underexpanded jet plumes, occur over a wider range than the range used for calibration. However, the calibration is expected to remain valid over the entire range due to the fundamental linear relationship between the molecular number density and the intensity of scattered light. Possible sources

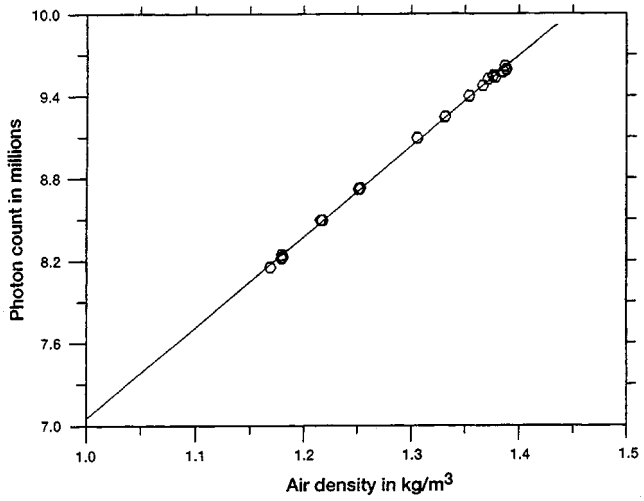

FIG. 2. Calibration curve of Rayleigh scattered light to measure air density. Straight line shows a least-square fit.

of deviation, such as a change in the molecular composition, is expected to be of little concern over the Mach number range encountered.

B. Validation

The density field of a fully expanded jet ($M_j = 0.99$) was measured to validate the measurement technique (Fig. 3). The same nozzle was used for calibration and all other data presented in this paper. The radial profiles were measured by moving the probe volume from point to point and performing a photon count at each point. The fundamental error source in the time-averaged measurements is due to the electronic shot noise (in the photomultiplier tube) which is manifested as the statistical photon count noise. The shot noise is proportional to the variance of the number of photons (N) detected over a fixed time interval in repeated measurements. Since the detection of photons obeys Poisson's statistics, the variance of the photon count is equal to the average number of counts, i.e., $\mathrm{var}(N) = N$, the relative uncertainty in the measurement of N is given by

$$\frac{(\mathrm{var}(N))^{1/2}}{N} = N^{-1/2}. \tag{7}$$

For the present experiment the count rate was high; over a 4 s interval the number counted was between 5 and 10 mil. Therefore, the uncertainty from the shot noise was below 0.05%. Since the contribution from the fundamental noise source was very low, that from a host of secondary sources became prominent. Occasional particles were unavoidable and their passage led to an increase in the photon count. There were very fine oil droplets, perhaps picked up from the air compressor, that caused a small difference in scattering intensity between the supply air and the cleaned ambient air. A third source of error was from a slow temperature drift of both supply and cleaned ambient air over 4–5 h of continuous operation. Usually, a calibration curve was obtained at the beginning or at the end of a day, and was used for all data acquired in that day. The secondary noise sources are difficult to quantify. It is expected that some of the sources lead to bias error and the others to random error (precision error). The calibration of photon arrival rate against known density value is expected to minimize the bias error. The random part of the uncertainty was estimated from repeatability of data. The measured data are found to be repeatable within $\pm 1\%$ of the quoted values.

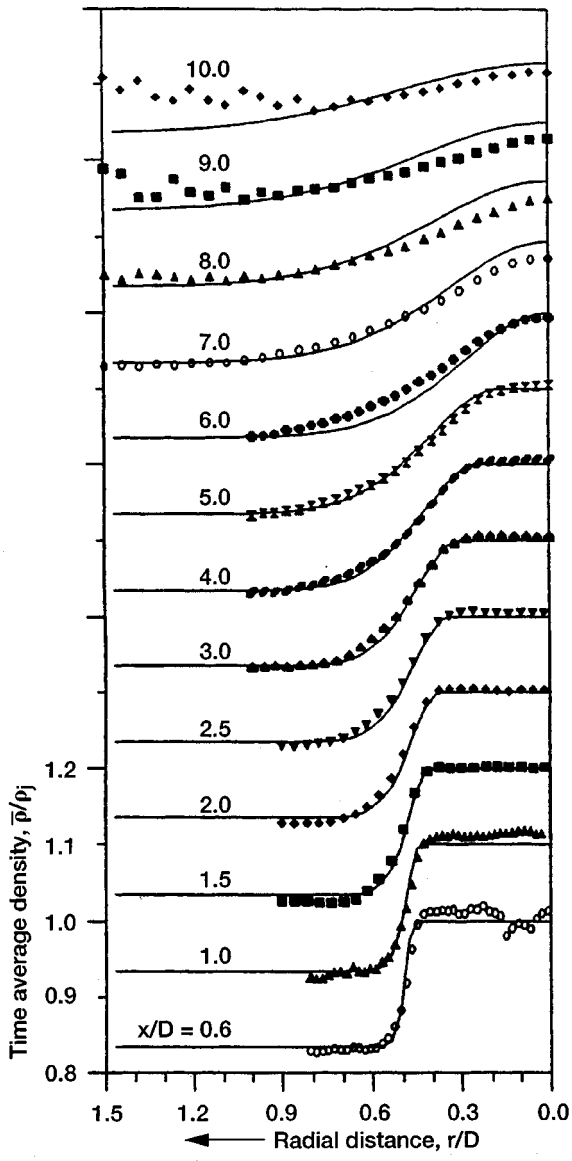

FIG. 3. Radial profiles of time-average density from indicated axial positions measured in $M_j = 0.99$ jet. Solid lines correspond to the expected variation. Each plot is shifted by a division.

The solid lines used in Fig. 3 are from a commonly used empirical relation to describe the density variation in correctly expanded free jets (Morris and Tam,[29] Tam *et al.*[30]). The relation relies on earlier measurements of axial velocity distribution in free jets and then density is calculated using Crocco's relation. The empirical relationship does not provide an exact description of density variation; however, in the absence of any other reliable density data in the literature, the empirical relation is used as a guideline. The details of the relationship are postponed to the Appendix. Perhaps

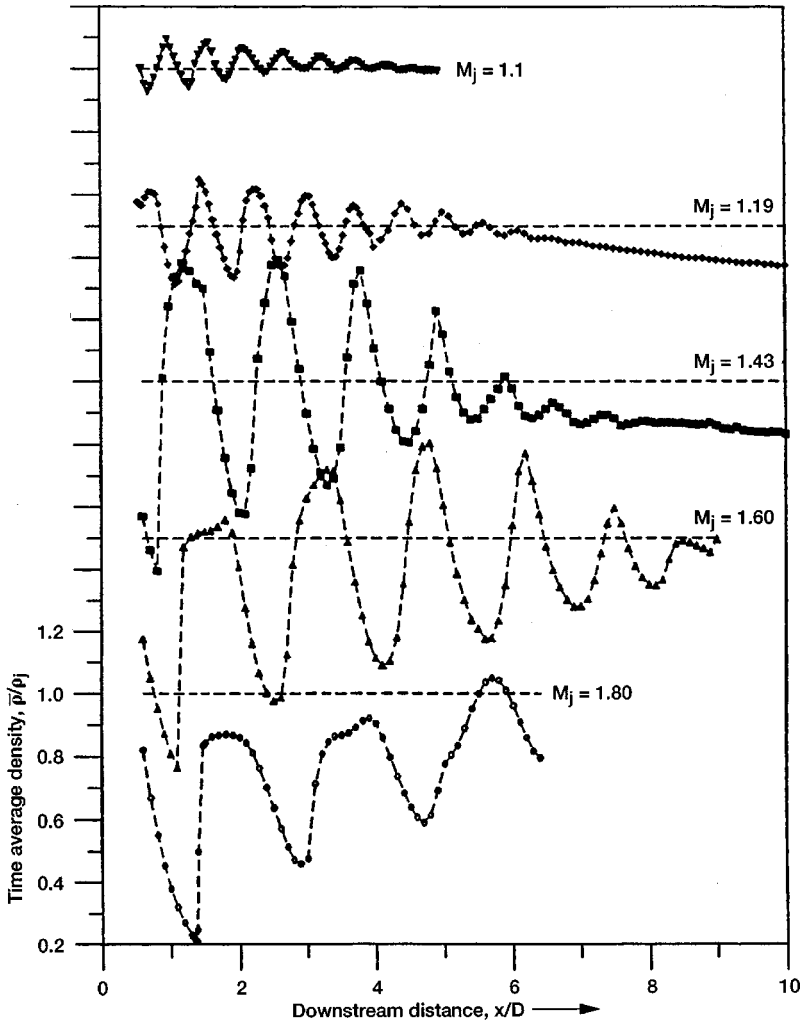

FIG. 4. Time-averaged, centerline density variation at indicated Mach numbers. The straight lines show the fully expanded density value, i.e., $\overline{\rho}/\rho_j = 1$. Each plot is shifted by five minor divisions.

the reliable part of the empirical relation is the description of the jet core that lasts up to $5D$ downstream distance. In this region, between $x/D = 1.5$ to 5, the measured data follows the expected variation with $\pm 1\%$ uncertainty limit. It has been already mentioned that the background illumination contaminated data up to $x/D < 1.5$. The no flow correction [Eq. (4)] produces some data scatter seen in the traverses at $x/D = 0.6$ and 1.0. A second problem region is the outer part of the shear layer beyond $x > 20$ cm ($x/D = 8.0$). The edge of the hood supplying clean air lies at this line. The dust-containing ambient air starts to entrain in the shear layer and contaminates data. Except for the problem regions, the additional discrepancies between the measured data and the empirical relations apparent in the shear layer region are believed to be due to the inaccuracy of the latter. Finally almost all time-averaged data, including Fig. 3, present only one-half of the jet. The symmetry was checked from additional measurements across the jet cross section[31] and found to be satisfactory.

C. Time-averaged data

As the plenum pressure is increased beyond the choked flow condition a series of shock cells form in the jet plume and the isentropic relation [Eq. (5)] no longer applies. The density variations measured along the jet centerline for five different levels of underexpansion are shown in Fig. 4. All density data presented in this paper are normalized by the ideally expanded density value, ρ_j, obtained by using Eq. (5). The straight lines in Fig. 4 correspond to these values. For the lower Mach number conditions (until a Mach disk forms in the jet core, around $M_j = 1.5$) the local density oscillates about ρ_j. It decreases below ρ_j in the expansion part of each shock cell and increases above ρ_j in the shock-compression part. The oblique shocks formed in the jet are weak and therefore, nonisentropic heating is minimum. The data presented for the $M_j = 1.80$ jet show a deviation where the local density does not rise over ρ_j after first few shocks. It is known that there occurs a large entropy generation downstream of a normal shock. The associated rise in temperature, beyond what is attainable by isentropic compression, is referred to as shock heating. Shock heating causes a lower value of density than what is attainable by isentropic compression. This feature also becomes clear from a comparison between the Rankin–Hugoniot and isentropic relations for density increase. The lowering in density due to shock heating becomes prominent as the strength of the

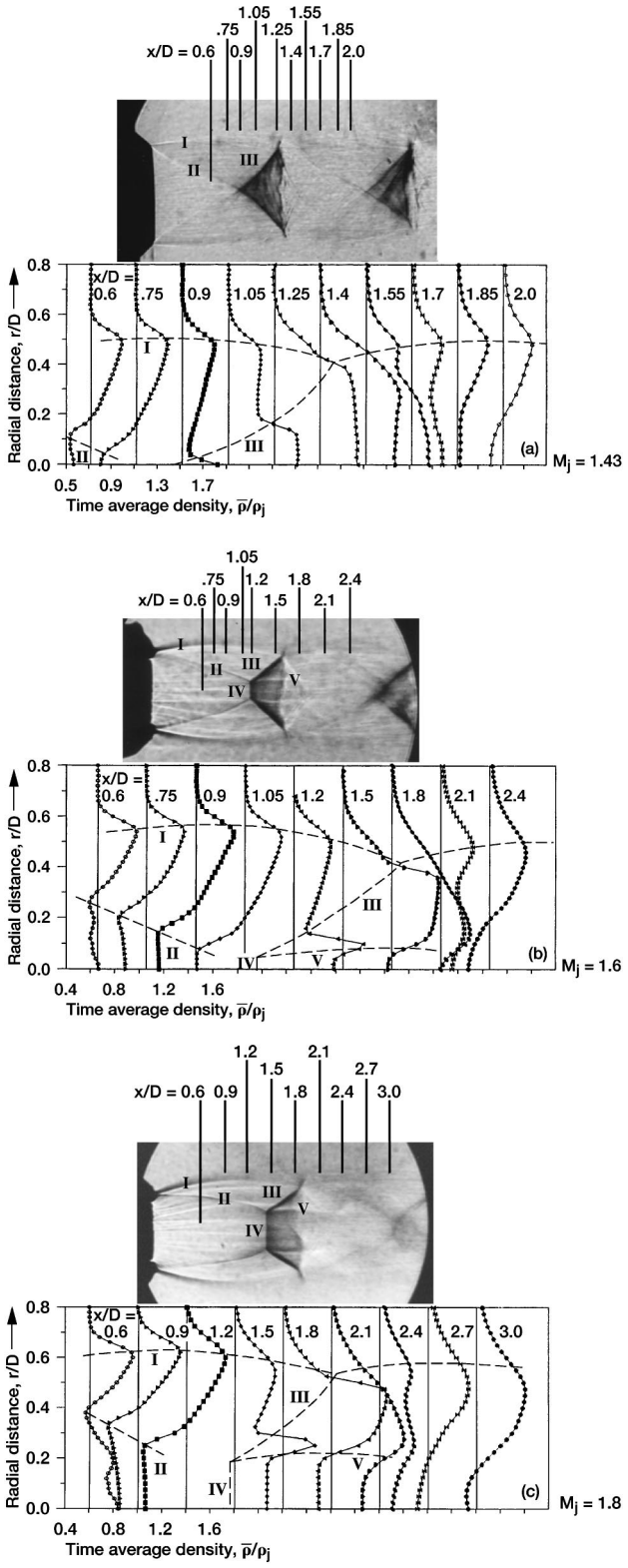

FIG. 5. Comparison of density measurement with schlieren photographs at three Mach no conditions (a), (b), (c). Streamwise distances (x/D) from the nozzle lip are marked. Solid base lines correspond to ambient density. Each plot is shifted by two minor division. The chain lines correspond to (I) inviscid boundary, (II) incident shock (or its inception), (III) conical shock or reflected shock, (IV) Mach disk, (V) slip stream.

Mach disk increases, as seen between $M_j=1.6$ and 1.8 jets. Mixing caused by a spreading of the slipstream eventually increases the local density, as apparent in the latter shock cells, yet the jet is changed due to a large entropy production after the Mach disk. In general, for all Mach number conditions, viscous losses and mixing dissipate the shock cells further downstream from the nozzle exit and progressively reduce air density to the ambient value.

Figure 5 shows the complex density variation around the first shock formed just after the nozzle exit. The following is an attempt to provide some insights into the variation. Note that the schlieren photographs and the density plots are not in the same scale and thus, for a comparison, one needs to match the axial positions marked in the photographs and the plots. Also note that the chain lines in the plots do not indicate exact locations to the indicated feature. The density data were obtained for one-half of the jet cross section. The inviscid jet boundary, indicated by the chain lines labeled I, nominally corresponds to ρ_j, the isentropically expanded density. The shear layer lies radially outside of this boundary. Inside the boundary lies various shock waves and slip stream as marked. The expansion region, just after the nozzle exit, causes density to fall below the ambient level. However, even inside this expansion region the inception of a weak shock, labeled II, is encountered. The weak shock shows up as a faint diagonal line originating from the nozzle lip in the schlieren photograph for the $M_j=1.43$ jet. As the degree of underexpansion is increased in the $M_j=1.6$ and 1.8 jets the diagonal line becomes curved and is known as the barrel shock or incidence shock (Adamson and Nichols[32]). It is interesting to note that an inception of the incidence shock can be noticed even in the schlieren photographs of the $M_j=1.1$ jet (not presented here). The incidence shock ends at the conical (or truncated conical) compression boundary. In the $M_j=1.43$ case the shock compression zone (marked III) is conical and density remains uniform inside the cone. For the higher Mach number conditions, however, a normal shock (Mach disk labeled IV) appears in the core. The Mach disk is accompanied by a shock triple point and a slipsteam (labeled V, Love *et al.*[4]). The slip stream is an axisymmetric imbedded shear layer that separates the subsonic, flow downstream of the Mach disk, and the supersonic flow downstream of the reflected shock (labeled III). The local density increases across the Mach disk; however, as mentioned earlier, excessive heating due to the nonisentropic compression produces a value lower than ρ_j. In the radial traverses made downstream of the Mach disk, such as at $x/D=1.5$ in Fig. 5(b) or at $x/D=1.8$ in Fig. 5(c), the probe volume progressively move outward from the centerline through the slip stream, downstream of the reflected shock, crosses the reflected shock, and passes through the shear layer. The local density is relatively high downstream of the Mach disk, however, it becomes even higher as the slip stream is crossed; the density drops to a smaller value in front of the reflected shock, and approaches the ambient condition through the shear layer. The axial direction further downstream of the shock-compression zone marks the beginning of another expansion process and the flow density is progressively reduced.

Before leaving this part it is useful to address the nature of density variation across shock waves formed in the underexpanded jet plumes. A closer look into the density variations for the moderately underexpanded jet (that is before the Mach disk formation, $M_j<1.5$), show relatively smooth increases in the compression regions (Fig. 4). This brings the question of whether shock waves are present at all, since the density data should show a sharp jump as opposed to the smooth increase across a shock. It is believed that there exist multiple causes whose combined effect results in the smoothening process. The first possibility is the spatial averaging associate with the finite probe volume; however, the probe volume is about 1 mm long, while the compression process may occur over more than 10 mm distance. The second reason is the shock oscillation. Panda[13] has shown that all but the first shock oscillates vigorously in a screeching jet, and such oscillation is the primary reason for the smoothening effect seen in all shocks formed downstream of the first one. Now, the first shock is measured to oscillate barely by less than 1 mm distance, which is insufficient to explain the slow compression over a 10 mm distance seen for the moderately underexpanded jets ($M_j<1.5$, Fig. 4). The first shock is also examined in Fig. 5, where the radial traverses show that even for the higher Mach number conditions of $M_j=1.6$ and 1.8 the density increases smoothly across the reflected shock (III). All of these point out the presence of additional physics, perhaps explainable in the light of Pack's[33] analysis. It is known that, in an underexpanded jet, expansion waves originate from the nozzle lip and reflect back from the jet boundary as compression waves. An examination of Pack's analysis indicates that a part of the compression waves forms the shock and the rest lie either in front of or cross the shock. Therefore, density is expected to show a slower increase in spite of the presence of a shock wave.

To model screech one needs to know the behavior of the surrounding shear layer and the decay of the shock cells present in the core. Figure 6 provides such a data set for the $M_j=1.19$ jet. Although radial traverses were made at a large number of axial stations, only a selected few are presented in Fig. 6 for the sake of clarify. Similar data for a few other Mach number conditions are also available from the authors. The solid lines in Fig. 6 show the expected density distribution in an ideal jet that is correctly expanded to 1.19 Mach number. The empirical relation used is described in the Appendix. Note that the abscissa in nondimensionalized by D_j, the fully expanded jet diameter which accounts for the increase in the effective diameter of an underexpanded jet:[34]

$$D_j=\frac{D}{\sqrt{M_j}}\left[\frac{1+\frac{1}{2}(\gamma-1)M_j^2}{1+\frac{1}{2}(\gamma-1)}\right]^{(\gamma+1)/4(\gamma-1)}. \tag{8}$$

The use of D_j, instead of the nozzle exit diameter, D, provides a better fit to the experimental data. The solid lines are representatives of the density profile used in the previous computational efforts for screech prediction,[5,9] while the experimental points show the actual variation present inside the jet. Inside the potential core, modulations from the shock cells causes significant deviations from the fully expanded jet conditions. Even the shear layer is found to develop differently, especially after $x/D=2$. Additional lobes in the shear layer indicate a second inflection point and show a significant increase in the shear layer spreading.

D. Phase-averaged measurement

The advantage of working on a screeching jet is that the unsteadiness in the jet column and the radiated sound waves appears primarily at the screech frequency. The shear layer around the jet periphery develops Kelvin–Helmhltz type instability waves that roll up into coherent vortical structures, which interact with the shock cells and produce the screech tone. Since all of these phenomena appear at the screech frequency, the powerful phase-averaging technique can be applied to provide a deterministic description of the complete process. The phase-averaged Rayleigh scattering measurements are reported here for the first time. The phase-averaging process separates the phase-locked coherent component for the background random turbulent fluctuations. The originally proposed phase-averaging process of Hussain and Reynods[35] used a triple decomposition. However, for the present application a double decomposition is used. The time-dependent density $\rho(x,r,t)$ is split into a phase-locked coherent component $\langle\rho\rangle(x,r,\tau)$ and an incoherent random fluctuation $\rho'(x,r,t)$:

$$\rho(x,r,t)=\langle\rho\rangle(x,r,\tau)+\rho'(x,r,t). \tag{9}$$

Here, τ is the phase time ($0\leqslant\tau\leqslant T$) that varies within the screech time period T. The phase-averaged density is defined as

$$\langle\rho\rangle(x,r,\tau)=\frac{1}{L}\sum_{i=1}^{L}\rho(x,r,\tau,t+t_i), \tag{10}$$

where the time reference t_i for the phase-averaged measurements was generated from the screech sound signal measured by a microphone placed in the vicinity of the jet. The time resolutions are 1/24 and 1/36 of the screech period for the $M_j=1.19$ and 1.42 jets, respectively, and the sample size L is 1000.

Since the time average of the incoherent fluctuation is zero, the time-averaged density can be calculated from the phase-locked component. The latter also provides a measure of coherent fluctuation, $\langle\rho\rangle_{\rm rms}(x,r)$,

$$\begin{aligned}\overline{\rho}(x,r)&=\frac{1}{T}\int_0^T\langle\rho\rangle d\tau,\\ \langle\rho\rangle_{\rm rms}(x,r)&=\sqrt{\frac{1}{T}\int_0^T[\langle\rho\rangle-\overline{\rho}]^2 d\tau}.\end{aligned} \tag{11}$$

In the present experiment density is measured by counting the number of photon pulses arriving within a given time interval. For the phase-averaged measurement such counting was performed over a gated time interval (Fig. 7). The width of the gate is typically 5 μs and the position of the gate from the falling edge of a trigger pulse can be adjusted by a suitable delay. Since the screech time periods are roughly 120 μs and 180 μs, the time resolution as mentioned earlier is achievable. For trigger generation from the screech tone a

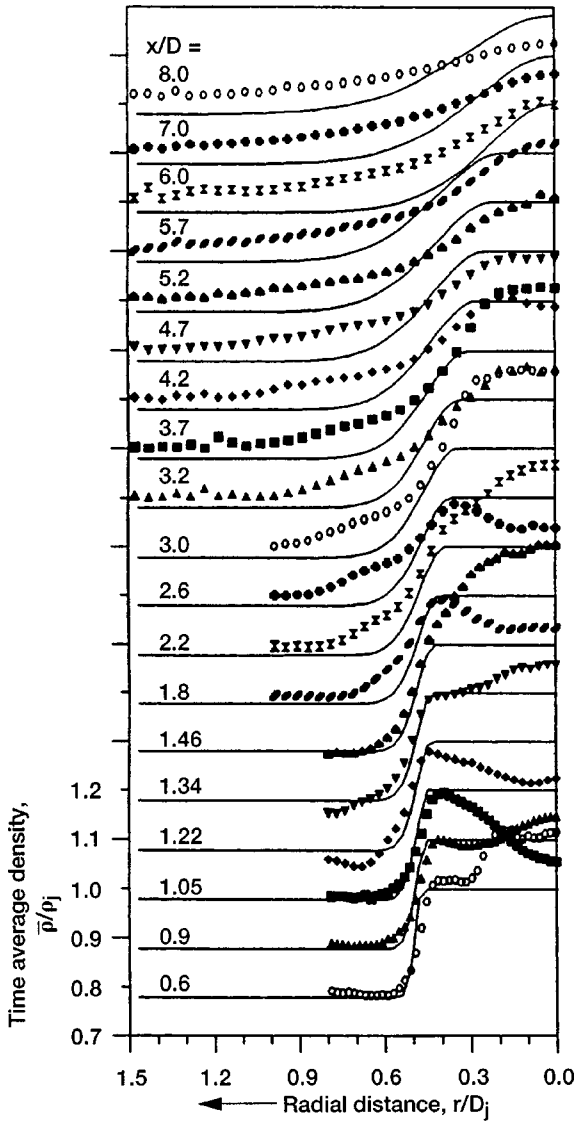

FIG. 6. Radial density profiles obtained at the indicated axial distances from the nozzle lip in underexpanded $M_j = 1.19$ jet. The solid lines show expected distribution in a fully expanded jet.

microphone was placed at the jet vicinity. In order to reduce triggering uncertainty from other random noise components, the microphone signal was bandpass filtered through a 1000 Hz window around the screech frequency. Usually the screech tone is very prominent, typically it stands out 20 dB above the random noise; therefore the bandpass filtering does not significantly change the signal. Subsequently, the bandpassed signal is fed into a wave form generator, where short duration TTL pulses are generated at the zero crossings with positive slopes. The series of TTL pulses are then used by the photon counter to generate gates for counting. The photon arrival rate at a particular phase is determined from the accumulated count over 1000 samples, and then converted into density using the calibration constants [Eq. (6)]. The phase-averaged data have higher uncertainty level than the time-averaged counterpart as the total time over which the photon count is accumulated is much less than the latter. Using Eq. (7) and the typical count rate, the estimated error contribution from the shot noise alone is $\pm 1\%$. However, the primary source of uncertainty arose from the unsteadiness of the supply air and inherent jitter in screech frequency. The central air supply served multiple installations and therefore, some amount of pressure fluctuation is unavoidable. However, data were taken only when the pressure remained steady within $\pm 1.5\%$ of the plenum pressure set point. Within this limit the screech frequency was found to change by about ± 75 Hz. There was also a naturally present unsteadiness of nearly the same magnitude due to the inherent jitter in screech generation.[28] No attempt was made to quantify the increased uncertainty due to the screech frequency variation. Qualitatively, frequency variation affects the trigger locations used for the phase-averaging process. The net effect is a smearing of the measured fluctuations, that is, the measured density difference between peak and valley of an instability wave is expected to be smaller than the actual value. A similar trend is expected in the root-mean-square data derived from the phase-averaged measurements. The phase-averaged data are found to be repeatable within 10% of the quoted value.

Data obtained by the phase-averaging process inside the shear layer of the $M_j = 1.42$ jet are shown in Fig. 8. The axial traverse was made at a radial location of $r/D = 0.63$, which was deliberately chosen to be outside the potential core so that the time-averaged data in Fig. 8(a) do not show any modulation caused by the shock cells. Nevertheless, the phase-averaged data show large, spatially periodic density fluctuations, which propagate downstream with the flow [Fig. 8(b)]. The motion becomes evident by following any peak region from one trace to the next. The fluctuations are due to the instability waves that roll up into large coherent eddies and are phased locked with the screech frequency. The density variation inside a compressible eddy has a similar appearance to that of a shock cell, that is, there exist a compression and an expansion zone. Interestingly, the expansion zones are relatively longer and the density gradient is smaller; in contrast, the compression regions steepen up and occasionally provide the appearance of a shock wave. One such instance in Fig. 8(b) is marked by an arrow. The data were obtained by averaging over 1000 cycles (in effect 1000 eddies), and therefore, a sharp shock front is expected to be somewhat smeared out due to the natural differences between the eddies. In spite of the smearing process, the sharp compression regions in Fig. 8(b) are conspicuous and one cannot eliminate the possibility of a shock wave inside an eddy. The direct numerical simulations of compressible shear layer by Lele,[36] Lee *et al.*,[37] and others have predicted the presence of ''eddy shocklets,'' whose behavior are somewhat similar to the above mentioned description.

The growth and decay of the organized vortices are best measured by calculating the rms of the phase-averaged data obtained at each measurement point [Eq. (11)]. Note that such data provide a measure of fluctuations that are phase locked with the trigger signal, that is the fluctuations occurring in the screech frequency and all of its harmonics. The contributions from all other frequencies are averaged out. Figure 8(c) provide such data for the $M_j = 1.42$ jet. Notably the evolution data show that in addition to the overall growth and decay, there are local modulations. The modulations are

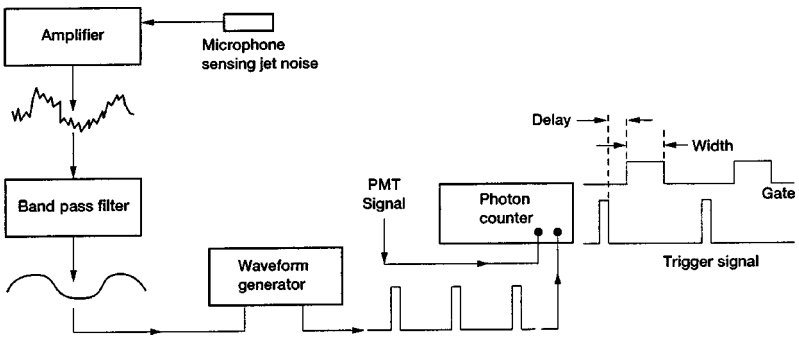

FIG. 7. A schematic of the phase-averaged photon counting arrangement for unsteady measurements.

the special feature of an incorrectly expanded jet and are not found in the fully expanded conditions. Previous measurements[11,38] using hot-wire probes also demonstrated such modulation; however, the present data are more reliable due to the nonintrusive nature of the Rayleigh scattering technique.

E. Combined density and near-field pressure fluctuation data

The axial traverse shown in Fig. 8 is at a fixed radial location. This is a subset of a large data set obtained from many axial traverses made at a large number of radial stations. The detailed data were obtained for two Mach number conditions: $M_j=1.19$ and 1.42 for which the screech tones are in, respectively, axisymmetric and helical modes. The global variations are shown in Figs. 9 and 10. In addition to the Rayleigh scattering data showing the density variation inside the jet, the near-field pressure fluctuations measured just outside the jet boundary and the convective speed (U_c) of the organized vortices measured in the shear layer are also combined in Figs. 9 and 10. The combined set is useful in correlating the modulations in all measured quantities. The density data are obtained from phase-averaged Rayleigh scattering measurements over a dense grid of 18 (in r)$\times$77 (in x) points for the $M_j=1.19$ jet and 20 (in r)$\times$80 (in x) points for the $M_j=1.42$ jet There is a pair of oblique strips in Figs. 9(c) and 10(c) where excessive background light contaminated the time-averaged density measurement; the affected data points are not shown. The time-averaged density and rms fluctuation values are calculated from the phase-averaged data following Eq. (11).

The pressure fluctuation data were obtained using a traversing microphone and has been described in an earlier paper (Panda[25]). In brief, a 3.18-mm-diam microphone was traversed from point to point over a grid of 53 axial and 19 radial positions for the $M_j=1.42$ case and 51$\times$21 stations for $M_j=1.19$ case. At each measurement point a narrow-band spectrum of the sound pressure fluctuation was obtained and the spectral peak at the screech frequency was measured. The spectral peak provided a measure of root-mean-square pressure fluctuation present at the screech frequency. All such measurements obtained from the complete grid are then plotted to obtain Figs. 9(a) and 10(a). The pressure fluctuation data of these two figures are quite complex The red-yellow node–antinode patterns, close to the jet boundary, are of particular interest as they indicate the presence of a standing wave and locations of possible sound sources. Further discussion of an interesting juxtaposition of similar node–antinode patterns inside the shear layer follows. The convective speed data are also from the same earlier paper; they were measured using a nonintrusive technique based on the line-of-sight scattering of a narrow laser beam by the organized vortices. The measurement technique, in brief, involved passing a narrow laser beam through the jet shear layer, normal to the flow direction, collecting the line-of-sight scattered light, and measuring by a PMT. The PMT output was cross correlated with the signals from a fixed microphone at the nozzle lip. The cross-correlation phase at the screech frequency is of interest. The relative change of the cross-correlation phase, as the laser beam was moved from point to point along the axial direction, was noted and the local convective speed is measured from the local gradient of phase variation. A quantitative description of the process can be found in Ref. 39. The convective speed (U_c) is normalized by the ambient sound speed (c) and is expressed as a convective Mach number, $M_c=U_c/c$. The purpose of the four plots in each of Figs. 9 and 10 is to relate the pressure fluctuation occurring outside the jet to the density and convective velocity fluctuation occurring inside. It is worth repeating that all rms measurement are of fluctuations occurring at the screech frequency.

Perhaps a discussion of shock noise should start with a description of the shock-cell structure. This is shown in Figs. 9(c) and 10(c) where the yellow-red regions represent shock compression and the blue-green regions correspond to the expansion part. As the Kelvin–Helmholtz instability waves, rolled up as organized vortices, are convected downstream by the flow their speed as well as the amplitudes are modulated. The rms density fluctuation plots of Figs. 9(b) and 10(b) show such modulation. An intriguing observation is the considerable difference in the axisymmetric and helical shock–vortex interaction presented in Figs. 9(b) and 10(b). The density fluctuation in the axisymmetric mode [Fig. 9(b)] takes the shape of a ladder. The poles of the ladder lie in the shear layer and the rungs lie in the expansion part of the shock cells. The appearance is different in the helical mode of Fig. 10(b). Nevertheless, from a sound generation point of view, the interest is in the fluctuation pattern observed in the shear layer where regular periodic modulations are apparent in both Mach numbers considered. The vertical chain lines in Figs. 9 and 10 indicate the positions of local maxima in turbulent fluctuations. An examination of the chain lines

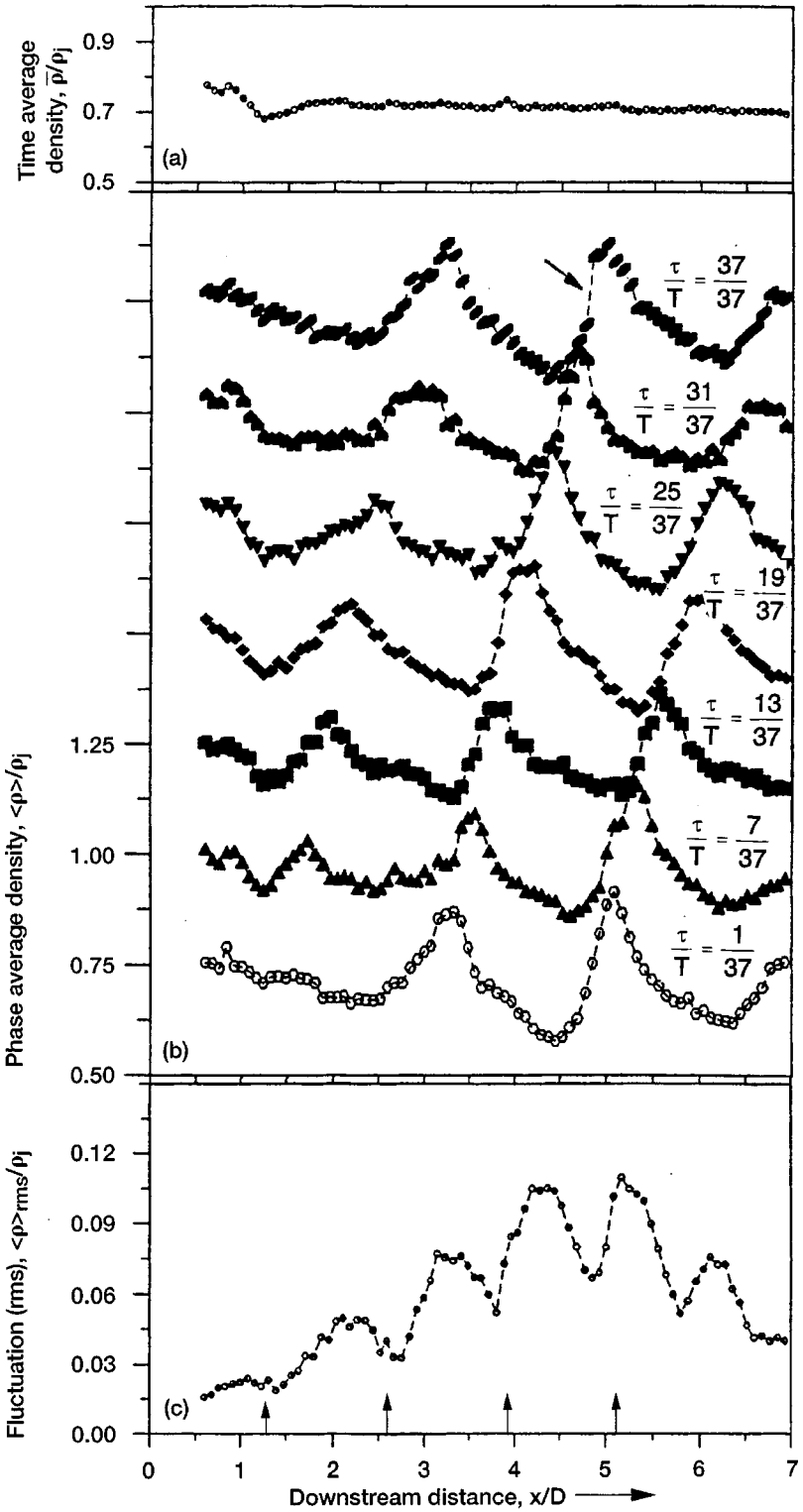

FIG. 8. Density variation in shear layer ($r/D=0.63$) of $M_j=1.42$ jet. (a) Time-averaged, (b) phase-averaged, and (c) root-mean-square fluctuations (coherent part). The vertical arrows in (c) indicate shock locations. Each trace of (b) is shifted by two minor divisions.

show that the locations of high convective speed [shown in Figs. 9(d) and 10(d)] matches those of local maxima in density fluctuation. In other words the locations of highest amplitudes are also the locations of the fastest speed of the organized eddies.

The vertical chain lines also line up with the antinode points in the near-field pressure fluctuation plots of Figs. 9(a) and 10(a). This provides a relationship between the modulation of the organized vortices and the screech sound generation process. As the organized vortices are periodically modulated, the pressure fluctuations follow suit and are manifested as the local maxima (yellow region) and minima (red region) in Figs. 9(a) and 10(a).

Standing waves inside the shear layer: At this point it is useful to bring the results of an earlier analysis[25] where it has

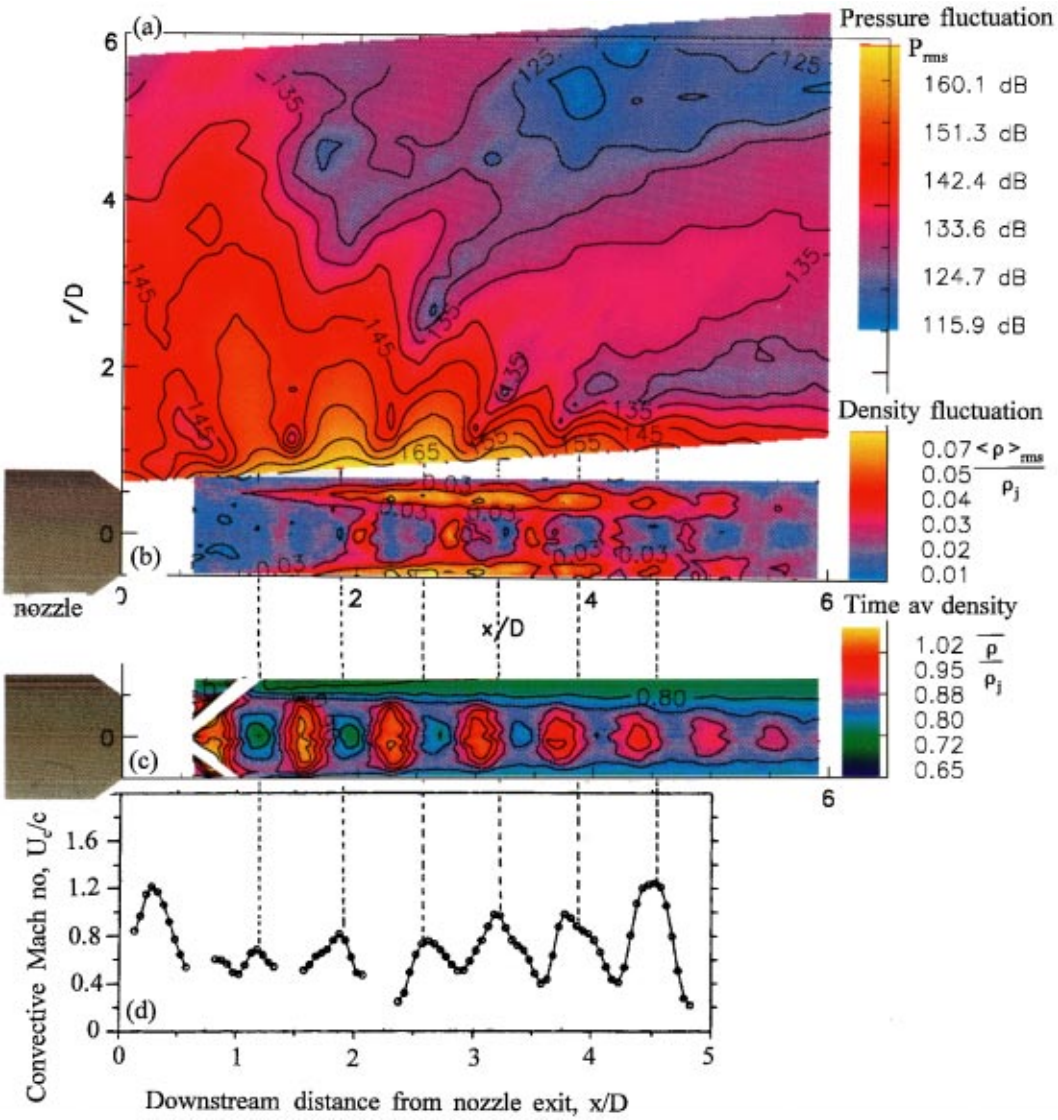

FIG. 9. Combined plots of (a) rms sound pressure levels at screech frequency, (b) rms density fluctuations (coherent part), (c) time-averaged density variation, and (d) convective speed of organized vortices at $r/D=0.48$ in $M_j=1.19$ jet. Vertical chain lines correspond to local maxima in convective speed.

been demonstrated that the local maxima and minima in the pressure fluctuation [Figs. 9(a), 10(a)] can be explained as the outcome of an interference between two wave systems. In a screeching jet the pressure field of the Kelvin–Helmholtz instability waves, also referred to as the organized vortices, interact with two additional wave systems. The first one is the stationary shock-cell system present inside jet core, and the second one is the upstream propagating screech waves generated from the shock–vortex interaction. In the literature the potential pressure field associate with the instability waves is referred to as the hydrodynamic field. The standing wave system, mentioned above, is produced by interference between the hydrodynamic fluctuations that propagate downstream and the sound waves that propagate upstream. If the wave systems are assumed to have uniform convective velocities, the wavelength associated with the instability waves is assumed to be λ_h, that with the sound waves is λ_s, then the standing wavelength L_{sw} satisfies the following:

$$\frac{1}{L_{sw}}=\frac{1}{\lambda_s}+\frac{1}{\lambda_h}. \tag{12}$$

Reference 25 shows that the node–antinode pattern in the near-field pressure fluctuation indeed satisfies this length scale. To arrive at Eq. (12), one of the assumption was uniform convective velocity for the instability waves. Figures 9(d) and 10(d), on the other hand, show extreme modulations. The difference is resolved by assuming an extension of the same standing wave inside the shear layer. It has been demonstrated by Panda *et al.*[39] that in a partially formed standing wave the local convective velocity show periodic modulations over an average value. If a standing wave is present in the shear layer then the modulated feature will be measured instead of the uniform velocity of the instability waves alone. Note that additional convective velocity data obtained from various radial locations in the shear layer show that the modulations are weakened in the inner part of the shear layer (toward the jet core) and strengthens in the

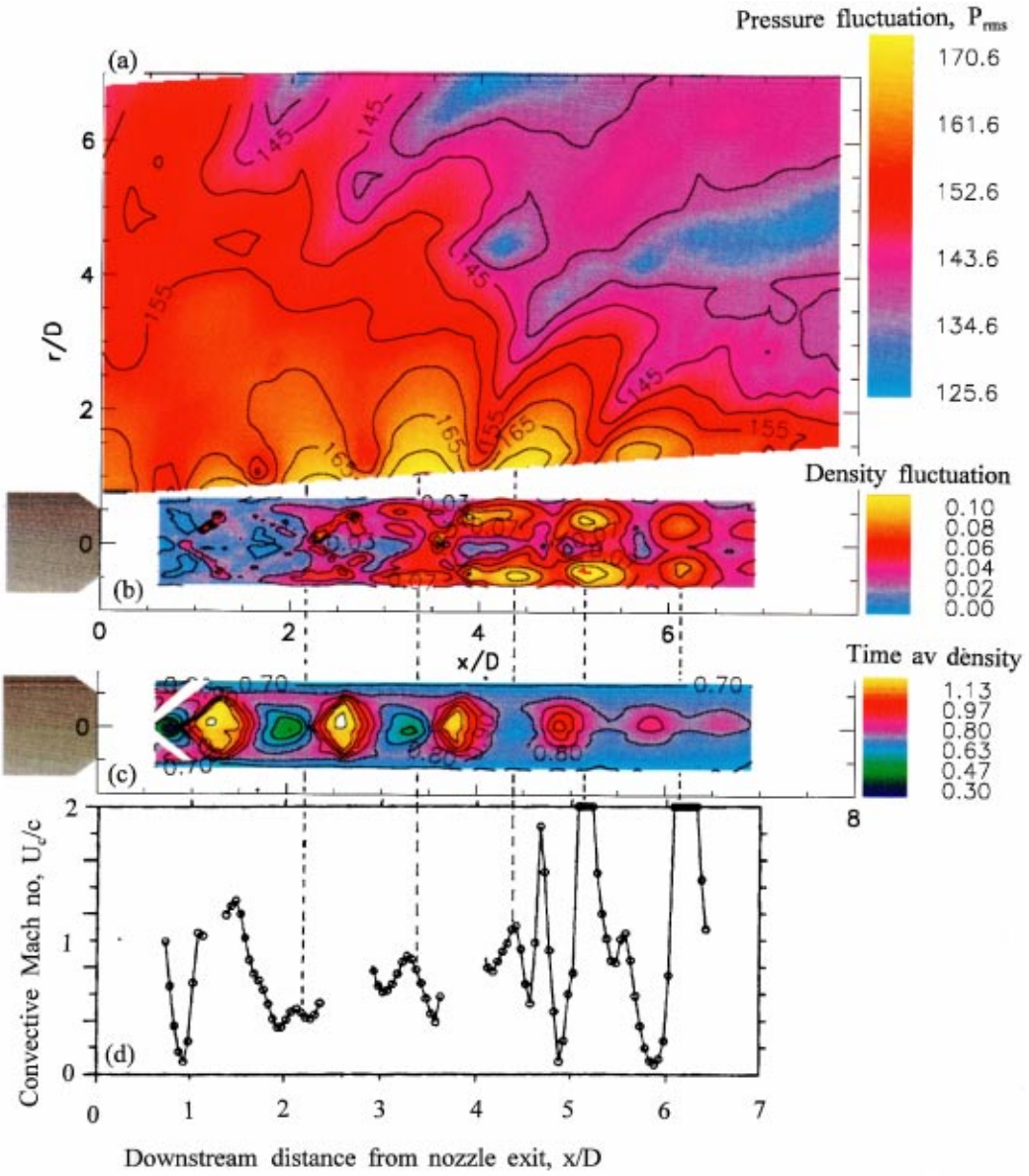

FIG. 10. Combined plots of (a) rms sound pressure level (P_{rms} in dB) at screech frequency, (b) rms density fluctuations (coherent part, $\langle\rho\rangle_{\mathrm{rms}}/\rho_j$), (c) time-averaged density variation ($\overline{\rho}/\rho_j$), and (d) convective speed of organized vortices at $r/D=0.48$ in $M_j=1.42$ jet.

outer part. The amplitude modulations of Figs. 8(c), 9(b), and 10(b) are also explainable in terms of the partially formed standing wave pattern. The local maxima in the density fluctuations correspond to the antinode and the minima to the node points of the standing wave.

To form a standing wave an upstream propagating disturbance needs to be present in the shear layer in addition to the instability waves. A direct proof of the existence of an upstream propagating disturbance cannot be obtained from the experimental data, since a separate measurement of the two wave systems is impossible to perform. However, recent computational efforts of Manning and Lele[7] provide the necessary proof. Through a direct numerical simulation of interaction between Kelvin–Helmholtz instability waves and an isolated shock they have shown that part of the generated screech sound wave propagates upstream through the shear layer as oblique Mach waves.

The above-mentioned analysis disregards an intuitive expectation that the shock cells are directly responsible for the amplitude and phase speed modulation of the instability waves. Figures 9 and 10 (and a host of data presented in Ref. 39) show that the periodicity of modulation of the instability waves is somewhat different from the shock spacing but close to the standing wavelength. For the $M_j=1.19$ and 1.42 jets L_{sw}/D is, respectively, 0.67 and 1.02, while the average shock spacing normalized by jet diameter is, respectively, 0.77 and 1.28.

That the sound waves affect the development of their own source, instability waves, shows the nonlinearity involved in the screech generation process. The nonlinearity may also explain an earlier observation that the use of the standing wavelength, as opposed to the shock spacing, provides the correct formulation to predict screech frequency. A

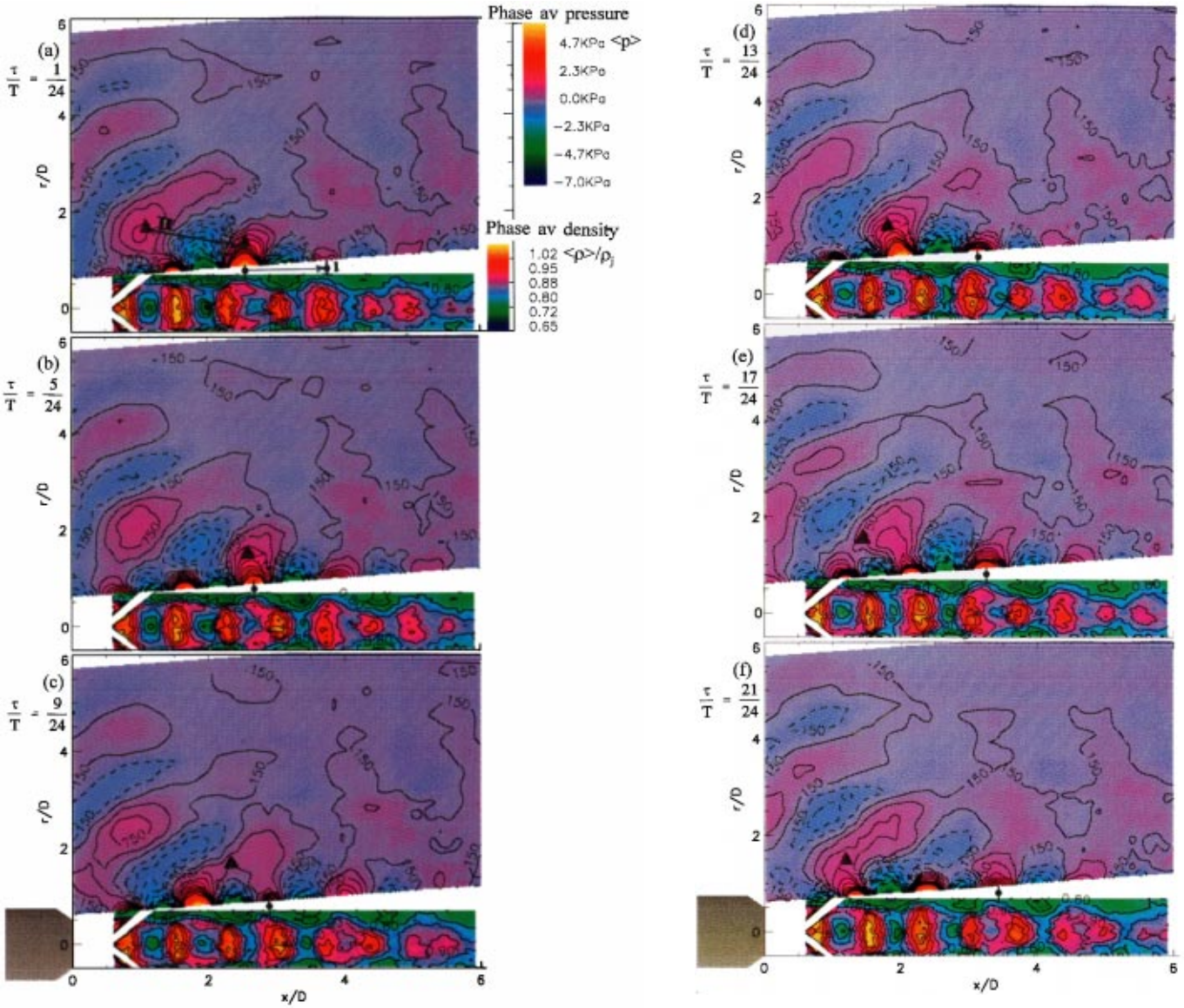

FIG. 11. Combined plots of phase-averaged sound pressure variation (top part) and phase-averaged density variation (bottom part) in $M_j = 1.19$ jet at indicated six different phases of screech cycle. The symbol ● connects one eddy in flow with its hydrodynamic field, the symbol ▲ shows compression part of a sound wave; arrows I and II show the distances covered by, respectively, an eddy and a sound wave over a screech cycle.

proper incorporation of this nonlinearity may also be critical in predicting screech amplitude via computational means.

Time evolution of density and pressure fluctuation obtained through phase averaging: Here we present extremely detailed, unsteady density and pressure field data that ultimately show time evolution of the shock–vortex interaction leading to the generation of the individual compression and rarefaction parts of the sound waves. This is the most fundamental way of looking into the sound generation process. Unlike the previous qualitative schlieren visualization,[27,25] Fig. 11 provides a quantitative description of the process. The videotape[40] accompanied by the paper was made from the same data sets and provides a better insight into the complex interaction process. There are two data sets used to create Fig. 11. The flow field information was obtained from phase-averaged density measurement. This part is new. The near-field pressure fluctuation was obtained from phase-averaged microphone measurement. This part was reported earlier in Ref. 25. Since the two sets were measured using two different techniques, a phase matching was necessary. This was accomplished by matching the phases of fluctuations occurring along the lower boundary of the pressure data and the upper boundary of the density data. The screech time period (T) in the $M_j = 1.19$ jet was divided into 24 phase intervals (τ), out of which only 6 phases that are nearly equally spaced are shown in Fig. 11. Similar measurements for a second Mach number condition of $M_j = 1.42$ was also performed. The shock–vortex interaction is somewhat different as the screech mode shape is helical. The video contains an animation of this second Mach number condition.

There are certain regions in each plot of Fig. 11 where no data are available. The fluctuations in the narrow wedge region between the microphone and Rayleigh data were too

high to be measured by a microphone and too low to be resolved by Rayleigh. A significant amount of background scattering prohibited measurement close to the nozzle exit and along the whiten arrowhead region. The contour levels in the pressure fluctuation data are at an interval of 300 Pa (N/m^2) and those in the density plot are at an interval of 0.05. Note that a density is normalized by ρ_j.

Figure 11 can be described as an interaction between three different entities: the stationary shock-cell structure, downstream propagating instability waves, and primarily upstream (there exists a weaker downstream component) propagating sound waves. Among these three, instability waves are seen both in density and microphone (hydrodynamic fluctuation) data. The shock cells appear as a quasiperiodic compression (yellow-red) and expansion (blue-green) zones associated with the shock-cell system. The density fluctuation from the instability waves can be detected as red blobs that convect over the shock train as the phase time progresses. The instability waves are axisymmetric and a cross-sectional view is visible in the figures. One such instability wave is marked with a closed circle with a small vertical line. The purpose of the vertical line is to associate the pressure fluctuation measured in the near field with the density fluctuation measured in the jet. Over a screech cycle, the instability waves move by one wavelength (shown by the arrow I), which is roughly twice the shock-cell spacing.

The pressure data are also complex and a detailed discussion can be found in the original Ref. 25. In brief, there are two systems of waves present in the near field. The hydrodynamic fluctuations associated with the instability waves are prominent close to the jet boundary, where they propagate downstream. The second system is due to the screech sound waves, which propagate upstream and become more distinguishable slightly away from the jet boundary. Each wave system is made of a compression (red) and a rarefaction (blue) region. By following the sequence of figures it can be seen that the acoustic waves are generated from the modulated hydrodynamic fluctuations. The closed triangles in Fig. 11 follow the generation of the compression part of a sound wave. The video animation is especially useful in demonstrating this feature. It should be pointed out that a quantitative separation between hydrodynamic and acoustic fluctuation is difficult to make as both are in the same frequency. However, the advantage of working with a screeching jet is that the two propagate in opposite directions; this has provided the basis for a qualitative separation made in the above discussion.

IV. SUMMARY AND CONCLUSIONS

(1) The time-averaged density was measured in the Mach number range of $0.99 \leqslant M_j \leqslant 1.8$. At first, the density variation within one shock-cell distance around the first shock closest to the nozzle exit was explored and compared with schlieren photographs. An underexpanded jet starts with an expansion process where density progressively decreases until the shock compression region is encountered where density jumps to a higher value. The measured data showed complex deviations from this simple textbook description. A shock-like discontinuity is found to germinate from the nozzle exit and is found to grow in strength as the Mach number is increased. This discontinuity ultimately results in a barrel shock[32] when a Mach disk forms inside the core ($M_j > 1.5$). The density variation downstream of the Mach disk shows complex variation due to the nonuniform shock heating and the presence of an imbedded shear layer (slip stream). The detailed data should be useful in validating shock-capturing ability of the computational fluid dynamics codes.

The centerline density traverses show the decay of the shock-cell structure and the asymptotic fall of the jet density to the ambient value. To demonstrate the shear layer behavior, many radial transverses covering a downstream distance of 8 jet diameters were performed for a few Mach number conditions. When compared with the expected variation in fully expanded jets the extra features became obvious. The shear layer is found to grow faster and the presence of additional inflectional points (different from those caused by the shock cells in the potential core) were detected.

(2) The underexpanded jets produced intense screech tones, and the density fluctuations occurring at the screech frequency were measured by the phase-averaging technique. The detailed field data obtained for the $M_j = 1.19$ (axisymmetric screech mode) and 1.42 (helical screech mode) demonstrated the evolution of instability waves (which roll up into organized eddies) and their interaction with the shock cells. Phase-averaged sound pressure fluctuation measured outside the flow boundary in an earlier study (Panda[25]) for the identical operating conditions were superimposed on the density fluctuation data to obtain further insight into the sound generation process. A video animation of the two data sets shows the propagation of organized vortices over the shock train and the generation of the individual compression and rarefaction parts of the sound waves.

(3) The root-mean-square density fluctuation measured from the phase-averaged data shows that the instability waves are periodically modulated along the jet shear layer. A comparison with earlier data shows that these locations coincide with the local maxima in the convective velocity as well as the antinode points in the near-field sound pressure fluctuations. All of these point out the local modulations as the source of screech generation. The amplitude and convective velocity modulations of the instability waves are explained through a partially formed standing wave that is present in the shear layer and is similar to the one found just outside the jet boundary.

Note. This paper is accompanied by a video tape titled, ''Screech generation from underexpanded jets.'' All data presented in this manuscript and used for the video are submitted for EPAPS deposit in $3\frac{1}{2}$ in. disks (quantity 2) as ASCII files. A README file in disk No. 1 describes the data structure.[40]

ACKNOWLEDGMENT

The authors would like to acknowledge the help of Wentworth T. John in setting up the optical system.

APPENDIX: DENSITY DISTRIBUTION IN A CORRECTLY EXPANDED FREE JET

The axial velocity U at any radial point r is dependent on the mixing layer width $2b$ and the radius of the uniform potential core H. It can be expressed as[29,30]

$$\frac{U}{U_j}=\frac{U_c}{U_j} \quad \text{for } r\leqslant H$$
$$=\frac{U_c}{U_j}\exp\left[-(\ln 2)\left(\frac{r-H}{b}\right)^2\right] \quad \text{for } r>H, \tag{A1}$$

where U_j is the isentropically expanded jet velocity in the potential core and U_c is the centerline velocity that progressively decays according to the following:

$$\frac{U_c}{U_j}=1 \quad \text{till the end of potential core, } x\leqslant x_c$$
$$=1-\exp\left(\frac{1.35}{1-x/x_c}\right) \quad \text{downstream of potential core.}$$

Here, x is the streamwise coordinate and x_c is the length of the potential core. The latter, nondimensionalized by the jet diameter, is expressed as

$$\frac{x_c}{D}=4.2+1.1M_j^2.$$

The half width of the mixing layer, b, is assumed to grow linearly from the nozzle lip to the end of the potential core:

$$b=\frac{1.2658x}{10.7}(1.0-0.273M_j^2) \quad \text{for } M_j<2.0.$$

The last variable, H, the radius of the potential core, is determined from a consideration of the conservation of axial momentum at every radial station:

$$\int_0^\infty \rho U^2 r\,dr=\tfrac{1}{2}\rho_j U_j^2 R^2,$$

where ρ_j is the uniform jet density inside the potential core, and R is the jet radius. The density variation in the above mentioned equation, as well as in the final solution is obtained using Crocco's equation:[41]

$$\frac{\overline{\rho}}{\rho_j}=\left[\frac{\gamma-1}{2}M_j^2\frac{U}{U_j}\left(1-\frac{U}{U_j}\right)+\frac{U}{U_j}+\frac{T_a}{T_r}\left(1+\frac{\gamma-1}{2}M_j^2\right)\left(1-\frac{U}{U_j}\right)\right]^{-1}, \tag{A2}$$

where T_a and T_r are, respectively, the ambient and plenum temperatures.

[1] M. D. Salas ''The numerical calculation of inviscid plume flow fields,'' AIAA Pap. **74**, 523 (1974).
[2] E. Venkatapathy and W. J. Feiereisen, ''3-D plume flow computations with an upwind solver,'' AIAA Pap. 88-3158 (1988).
[3] J. M. Seiner, S. M. Dash, and D. E. Wolf, ''Shock noise features using the SCIPVIS code,'' AIAA Pap. 83-0705 (1983).
[4] S. M. Dash, in *Tactical Missile Aerodynamics, Progress in Astronautics and Aeronautics*, edited by M. J. Hemsch and J. N. Nielsen (AIAA, New York, 1986), Vol. 104, pp. 778–8941; E. S. Love, C. E. Grisby, L. P. Lee, and M. Woodling, ''Experimental and theoretical studies of axisymmetric free jets,'' NASA Tech. Report No. R-6 (1959).
[5] A. B. Cain, W. W. Bower, S. H. Walker, and M. K. Lockwood, ''Modeling supersonic jet screech. 1. Vortical instability wave modeling,'' AIAA Pap. **95**, 506 (1995).
[6] H. Shen and C. K. W. Tam ''Numerical simulation of the generation of the axisymmetric mode jet screech tones,'' AIAA Pap. 98-0283 (1998).
[7] T. A. Manning and S. K. Lele, ''Shock vortex interaction in supersonic jet screech: An update, 1998 ASME Fluids Engineering Division Summer Meeting (unpublished), FEDSM98-5238.
[8] A. Powell ''On the mechanism of choked jet noise,'' Proc. Phys. Soc. London **66**, 1039 (1953).
[9] C. K. W. Tam, K. K. Ahuja, and R. R. Jones, ''Screech tones from free and ducted supersonic jets,'' AIAA J. **32** (5), (1994).
[10] T. D. Norum and J. M. Seiner ''Measurement of static pressure and far field acoustics of shock-containing supersonic jets,'' NASA Tech. Memo 84521 (1982).
[11] T. F. Hu and D. K. McLaughlin, ''Flow and acoustic properties of low Mach number underexpanded supersonic jets,'' J. Sound Vib. **141**, 485 (1990).
[12] P. L. Eggins and D. A. Jackson, ''Laser-Doppler velocity measurements in underexpanded free jet,'' J. Phys. D **7**, 1894 (1974).
[13] J. Panda, ''Shock oscillation in underexpanded screeching jets,'' J. Fluid Mech. **363**, 173 (1998).
[14] C. Ross, L. M. Lourenco, and A. Krothapalli, ''Particle image velocimetry measurements in a shock-containing supersonic flow,'' AIAA Pap. 94-0047 (1994).
[15] M. P. Wernet, ''Fuzzy inference enhanced information recovery from digital PIV using cross-correlation combined with particle tracking,'' NASA Tech. Memo 106896 (1995).
[16] R. G. Seasholtz, F. J. Zupanc, and S. J. Schneider, ''Spectrally resolved Rayleigh scattering diagnostic for hydrogen-oxygen rocket plume studies,'' J. Propul. Power **8**, 935 (1992).
[17] W. M. Pitts and T. Kashiwage, ''The application of laser-induced Rayleigh scattering to the study of turbulence mixing,'' J. Fluid Mech. **141**, 391 (1984).
[18] S. C. Graham, A. J. Grant, and J. M. Jones, ''Transient molecular concentration measurements in turbulent flows using Rayleigh light scattering,'' AIAA J. **12**, 1140 (1974).
[19] F. C. Gouldin and R. N. Halthore, ''Rayleigh scattering for density measurements in premixed flames,'' Exp. Fluids **4**, 269 (1986).
[20] K. Fiedler, O. Sieber, and C. Jakiel, ''Quantitative density measurements by Rayleigh scattering behind a plane turbine cascade,'' AIAA J. **35**, 1303 (1997).
[21] G. S. Elliott and M. Samimy, ''Rayleigh scattering technique for simultaneous measurements of velocity and thermodynamic properties,'' AIAA J. **34**, 2346 (1996).
[22] N. D. Finkelstein, W. R. Lempert, and R. B. Miles, ''Cavity locked, injection seeded, titanium: Sapphire laser and application to ultraviolet flow diagnostics,'' AIAA Pap. 96-0177 (1996).
[23] J. A. Lock, R. G. Seasholtz, and W. T. John, ''Rayleigh–Brillouin scattering to determine one-dimensional temperature and number density profiles of a gas flow jet,'' Appl. Opt. **31**, 2839 (1992).
[24] R. B. Miles, J. Connors, E. Markovitz, P. Howard, and G. Roth, ''Instantaneous supersonic velocity profiles in an underexpanded sonic air jet by oxygen flow tagging,'' Phys. Fluids A **1**, 389 (1989).
[25] J. Panda, ''An experimental investigation of screech noise generation,'' J. Fluid Mech. **378**, 71 (1999).
[26] P. A. Lush and R. H. Burrin, ''An experimental investigation of jet noise variation with velocity and temperature,'' Technical Report Air Force Aero Propulsion Laboratory AFAPL-TR-62-53, Vol. 5.
[27] R. Westley and J. H. Woolley, ''Flow and sound visualization of an axisymmetric choked jet,'' 16mm Cine Films, No. 13 (1968), No. 20 (1970), NRC/NAE library.
[28] M. G. Davis and D. E. S. Oldfield, ''Tones from a choked axisymmetric jet. I. Cell structure, eddy velocity and source locations,'' Acustica **12**, 257 (1962).
[29] P. J. Morris and C. K. W. Tam, AIAA Pap. 77-1351 (1977).
[30] C. K. W. Tam, J. A. Jackson, and J. M. Seiner, ''A multiple-scale model of the shock-cell structure of imperfectly expanded supersonic jets,'' J. Fluid Mech. **153**, 123 (1985).
[31] J. Panda and R. G. Seasholtz, ''Velocity and temperature measurement in

supersonic free jets using spectrally resolved Rayleigh scattering,'' AIAA Pap. 99-0296 (1999).
[32]T. C. Adamson and J. A. Nicholls, ''On the structures of jets from highly underexpanded nozzles into still air,'' J. Aerosp. Sci. **26**, 16 (1959).
[33]D. C. Pack, ''On the formation of shock-waves in supersonic gas jets (two-dimensional flow),'' Q. J. Mech. Appl. Math. **I**, 451 (1948).
[34]C. K. W. Tam and H. K. Tanna, ''Shock associated noise of supersonic jets from convergent-divergent nozzles,'' J. Sound Vib. **81**, 337 (1981).
[35]A. K. M. F. Hussain and W. C. Reynolds, ''The mechanics of an organized wave in turbulent shear flow,'' J. Fluid Mech. **41**, 241 (1970).
[36]S. K. Lele, ''Direct numerical simulation of compressible free shear flows,'' AIAA Pap. 89-0374 (1989).
[37]S. Lee, S. K. Lele, and P. Moin, ''Eddy shocklets in decaying compressible turbulence,'' Phys. Fluids A **3**, 657 (1991).
[38]G. Raman and E. J. Rice, ''Instability modes excited by natural screech tones in a supersonic rectangular jet,'' Phys. Fluids **6**, 3999 (1994).
[39]J. Panda, G. Raman, and K. B. M. Q. Zaman, ''Underexpanded screeching jets from circular, rectangular and elliptic nozzles,'' AIAA Pap. 97-1623 (1997).
[40]See EPAPS Document No. E-PHFLE6-11-017912 for data and video files. This document may be retrieved via the EPAPS homepage (http://www.aip.org/pubservs/epaps.html) or from ftp.aip.org in the directory /epaps/. See the EPAPS homepage for more information.
[41]F. M. White, *Viscous Fluid Flow* (McGraw-Hill, New York, 1973).